Variations of Martian Proton Aurora in Different Timescales

J.-Y., Wu[1,2], *(yvonnewu@mail.iggcas.ac.cn)*, **F., He[1,2],** *(Corresponding author: hefei@mail.iggcas.ac.cn),* **Y.-J., Zhou[3], J.-W, Gao[1,2], L.-M, Yan[1,2], Z.-J, Rong[1,2], Y., Wei[1,2]**

1. Key Laboratory of Planetary Science and Frontier Technology, Institute of Geology and Geophysics, Chinese Academy of Sciences, Beijing, China.

2. School of Earth and Planetary Sciences, University of Chinese Academy of Sciences, Beijing, China.

3. Weihai Institute for Interdisciplinary Research, Shandong University, Weihai, China.

Introduction:

Proton aurorae are the most prevalent aurora type on Mars (Deighan et al., 2018; A. Hughes et al., 2019; Ritter et al., 2018), primarily occurring on the dayside. In contrast, electron aurorae, including discrete (Bertaux et al., 2006; Schneider et al., 2021)and diffuse types (Schneider et al., 2015, 2018), typically appear on the nightside. The hydrogen corona encompasses the Martian magnetosphere, which features a bow shock analogous to that of Earth. The position of the bow shock is influenced by the solar wind, causing the hydrogen corona to be variably exposed to solar wind particles (Halekas, Lillis, et al., 2015). While the induced magnetic fields deflect some solar wind protons, a fraction undergoes charge exchange, becoming energetic neutral atoms (ENAs). These ENAs can penetrate the bow shock and Magnetic Pileup Boundary (MPB), interacting further with atmospheric CO_2 and undergoing de-excitation, which produces Doppler-shifted Lyman-alpha (Ly-α) emissions—the signature of proton aurorae (A. Hughes et al., 2019). Unlike electron aurorae, which result from atmospheric excitation, proton aurorae originate from precipitating solar wind particles. This mechanism explains why proton aurorae are rarely observed on the nightside (Kallio & Barabash, 2001) and why the H Ly-α emission at 121.6 nm serves as an unambiguous diagnostic for identifying proton aurorae (Deighan et al., 2018).

In addition to ENAs, direct precipitation of energetic solar wind protons can also generate proton aurorae (Chaffin et al., 2022; He et al., 2023). Proton aurorae are strongly modulated by upstream solar wind. Notably, intense events are often linked to corotating/stream interaction regions (CIRs/SIRs) and coronal mass ejections (CMEs) at Mars (Ritter et al., 2018; Yun et al., 2022), which can enhance both auroral intensity and atmospheric ion escape (Jakosky, Grebowsky, et al., 2015). Proton aurorae typically peak near the southern summer solstice and are mainly influenced by solar wind flux, hydrogen corona density, and lower neutral atmospheric conditions (Deighan et al., 2018; A. Hughes et al., 2019). However, most of these results are based on data from 2014 to 2018.

In this study, we extend the dataset coverage from 2014 to 2024, providing nearly a full solar cycle of proton aurora observations from the MAVEN spacecraft. This expanded dataset enables us to examine auroral variability across three characteristic timescales: the ~26-day Carrington rotation, the Martian seasonal cycle (via solar longitude, L_S), and the solar cycle. In particular, we assess whether proton aurorae show consistent enhancement patterns across adjacent Carrington rotations, and how their intensity evolves through perihelion and southern summer solstice. By integrating seasonal and solar activity effects, we aim to refine the understanding of solar wind–Mars interactions across multiple timescales.

Data and Methods:

In this study, we use data from the Imaging Ultraviolet Spectrograph (IUVS) (McClintock et al., 2015) onboard the Mars Atmosphere and Volatile Evolution (MAVEN) spacecraft (Jakosky, Lin, et al., 2015). Specifically, we analyze processed Level 1C Far-Ultraviolet (FUV; 110–190 nm) limb scan data obtained near periapsis to generate altitude–intensity profiles and identify both the peak intensity and enhancement of Martian proton aurorae.

Our dataset spans from October 18, 2014, to May 9, 2024 (MAVEN orbits 109-21165), covering Martian Years (MYs) 32 to 37 and including the declining phase of Solar Cycle 24 and the ascending phase of Solar Cycle 25. Gaps in the data, primarily due to nightside limb observations and safe-mode events (Halekas, Taylor, et al., 2015), occurred notably from November 2018 to April 2019 and from March to September 2022. These discontinuities limit temporal continuity, particularly for long-term trend analysis.

We adopted a combined detection method based on Hughes et al. (A. Hughes et al., 2019) and He et al. (He et al., 2023) to identify proton aurorae. The dataset was divided into two altitude bands: 160–200 km (high-altitude background) and 110–150 km (peak-altitude region). From each orbit's altitude–intensity profile, we extracted the peak intensity and calculated the enhancement as the difference between the second-highest intensity within the peak-altitude region and the median intensity in the high-altitude background. The second peak was used to reduce the influence of local anomalies or environmental noise on the first peak, which can otherwise yield artificially large enhancements. An observation was classified as a proton aurora detection if the en-

hancement exceeded a statistically defined threshold (A. Hughes et al., 2019). Owing to proton auroral intensity strongly depending on solar zenith angle (SZA), we normalized each orbit to an SZA of 45° using a cosine-squared function of the form

$$f(x) = a \times \cos^2 (b \times x + c) + d,$$

where x is SZA and a-d are empirical parameters derived from intensity/enhancement-SZA profiles, following the method of He et al. (2023).

Column dust optical depth (CDOD) data were obtained from the Mars Climate Database (MCD) project (L. Montabone et al., 2015; Luca Montabone et al., 2020). We used the 9.3 μm CDOD product at a 6° longitude × 5° latitude spatial resolution and a Martian day temporal resolution. This study includes data from MYs 32, 33, 35, and 36. Although MY 34 featured a global dust storm, proton aurora observations during that period were limited by instrumental constraints, so MY 34 was excluded to avoid bias in the dust–aurora relationship.

Solar activity levels were characterized using extreme ultraviolet (EUV) flux from the EUV Monitor (Eparvier et al., 2015), a component of MAVEN's Langmuir Probe and Waves (LPW) instrument suite. The EUV monitor, mounted on the upper deck, maintains near-continuous solar orientation, enabling high-quality daily full-spectrum measurements used in this study.

Solar wind data were sourced from the Solar Wind Ion Analyzer (SWIA) instrument aboard the MAVEN spacecraft (Halekas, Taylor, et al., 2015; Liu et al., 2021). Due to the precession of MAVEN's elliptical orbit, continuous upstream coverage was not always possible. We therefore applied the filtering method developed by Gruesbeck et al. (2018) to identify intervals when MAVEN was outside the bow shock. To align solar wind data with proton aurora observations, we calculated the SZA in the MSO coordinate system using

$$SZA = \arccos\left(x / (x^2 + y^2 + z^2)^{1/2}\right),$$

and retained data within the range of 45° ± 2.5°. To reduce local variability, solar wind parameters were averaged over each MAVEN orbit. To study periodic responses across Carrington rotations, we defined the start of each rotation as day zero. Relative Carrington day was then calculated for each measurement by subtracting the start time from the timestamp, which enables direct comparison of repeating features in consecutive rotations.

To supplement MAVEN's solar wind dataset, we incorporated density and velocity measurements from the Mars Express (MEX) spacecraft (Chicarro et al.). Using these parameters, we calculated the corresponding dynamic pressure as

$$p = nmv^2,$$

where n is proton number density, m is proton mass, and v is solar wind velocity (Baumjohann & Treumann, 2006). Although MEX and MAVEN track similar large-scale trends, systematic differences exist in absolute values. Therefore, we used MAVEN as the baseline and applied a fitting procedure to adjust MEX data for consistency with our auroral observations.

Result:

In this study, proton aurora data are normalized to the point in each orbit where the SZA reaches 45°, and solar wind measurements are averaged over the same orbital period. Consequently, both datasets share a temporal resolution equivalent to a single MAVEN orbit (~4 hours). In contrast, EUV flux and CDOD data are provided as daily averages (24 hours). This multi-resolution framework facilitates the investigation of proton auroral variability across a broad range of timescales: from the ~4-hour orbital cadence, to the 26.35-day Martian Carrington rotation (CR), through seasonal changes over a full Martian year, and extending to the nearly 11-year solar cycle.

Variations in Carrington Rotation. We performed Fourier transforms on the complete time series of solar wind density, velocity, and EUV flux, identifying a dominant periodicity of 26.35 days, consistent with the solar rotation period as observed from Mars. This confirms the applicability of our proton aurora–Carrington rotation analysis to other rotations.

Using the start time of Carrington rotation 2184 (16 November 2016, 17:35:58 UTC) as day 0, we calculated the relative day within each 26.35-day rotation for all measurements. The same method was applied to Carrington rotation 2185, enabling time-aligned comparison across rotations, as shown in Figure 1.

In Figure 1(a), solar wind speed displays clear peaks near days 5 and 18, suggesting recurring coronal hole high-speed streams across the two rotations. In the shaded interval I (around day 1), proton auroral intensity in Carrington rotation 2185 closely follows the solar wind speed, density, and dynamic pressure. In Carrington rotation 2184, solar wind density and pressure align similarly, while the speed peak is slightly shifted, indicating a corresponding auroral enhancement.

In shaded interval II (around day 5), both rotations show comparable peaks in proton auroral intensity and solar wind dynamic pressure. In Carrington rotation 2184, the auroral peak appears to be mainly driven by solar wind density; in rotation 2185, it correlates more strongly with wind speed. Notably, the intensity peak in interval II is lower than in interval I, despite higher wind speeds, due to reduced density and dynamic pressure. This highlights the greater sensitivity of proton auroral intensity to solar wind density and pressure than to velocity alone. Together, intervals I and II illustrate consistent auroral responses to solar wind variability across consecutive Carrington rotations.

Shaded interval III spans days 14–19, corresponding

to the rising phase of the solar wind speed peak near day 18. In Carrington rotation 2184, three distinct peaks in auroral intensity, density, and pressure are observed. As solar wind speed increases, dynamic pressure peaks grow stronger, but the intensity and density peaks diminish, again suggesting that auroral intensity is more closely tied to density. In contrast, Carrington rotation shows only one significant peak set, centered on the second sub-interval. Here, the first auroral peak aligns with a density increase, and the third with a speed increase. All peaks in rotation 2185 are weaker than those in 2184, underscoring inter-rotational variability. Interval III further demonstrates that solar wind variability during similar temporal windows in consecutive rotations can lead to different auroral outcomes.

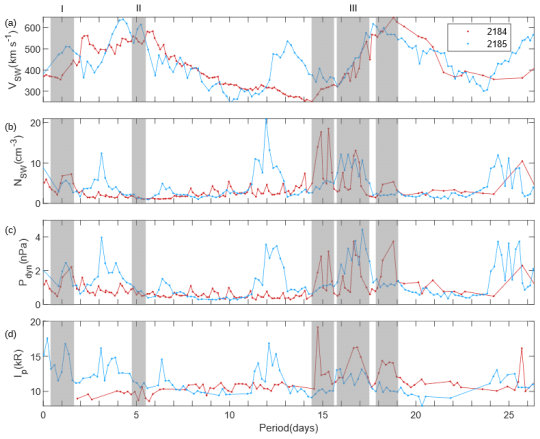

Figure 1. Comparison of solar wind parameters and proton auroral intensity during Carrington rotations 2184 (red) and 2185 (blue). The x-axis indicates the day number within each 26.35-day Carrington rotation. Panels (a)–(c) show solar wind speed, density, and dynamic pressure, respectively. Panel (d) displays proton auroral intensity. Shaded regions highlight time intervals where similar features appear in both Carrington rotations.

Variations in Martian Seasons. We divided the EUV flux, CDOD, solar wind density, and proton auroral intensity and enhancement into 360 bins at 1° intervals in solar longitude L_S, averaging values within each bin to produce Figure 2. The dataset spans Mars Years 32, 33, 35, and 36, matching the coverage of the CDOD dataset. Daily-mean EUV flux shows a general rise from L_S ~ 0° to 237°, followed by a decline from L_S ~ 237° to 360°, reflecting the ~27-day modulation of solar EUV flux (Thiemann et al., 2018), with a pronounced maximum between L_S ~ 185° and 237°.

CDOD data, resolved at 5° latitude, reveal three main dust-active regions: (1) L_S ~ 225°–254° and (2) L_S ~ 318°–342° in the 45° S to 45° N, and (3) L_S ~ 263°–278° in the 45° S to 90° S, corresponding to three characteristic types of Martian dust storms(Kass et al., 2016). Solar wind density and auroral parameters, normalized to SZA = 45°, all exhibit peak values between L_S ~ 237° and 307°.

The shaded region in Figure 2 connects the peak intervals of all five variables, revealing a clear sequence: peak EUV flux is followed by enhanced dust activity, which lifts and heats the atmosphere, raising daytime temperatures by up to 40 °C from 20° N to the South Pole (Kass et al., 2016; Smith, 2002), and promoting molecular motion. Solar wind density also peaks near perihelion, resulting in maximum proton auroral intensity and enhancement between perihelion and the southern summer solstice (L_S ~ 270°). While previous studies (A. Hughes et al., 2019) identified intensity peaks near solstice, our expanded dataset—twice the size of earlier work—shows that the interval spanning perihelion through solstice consistently features the strongest auroral responses. This highlights Mars's proximity to the Sun at perihelion as a key driver of proton aurora generation.

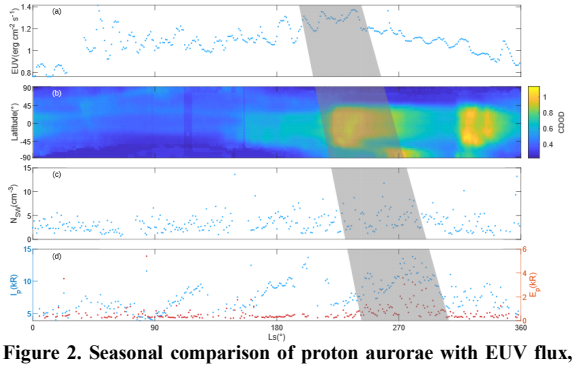

Figure 2. Seasonal comparison of proton aurorae with EUV flux, CDOD, and solar wind density, based on data averaged over Martian Years 32, 33, 35, and 36. The x-axis denotes L_S. (a), (c) and (d) show Daily-mean EUV flux, Solar wind proton density, Proton auroral intensity (blue dots), and enhancement (red dots) as a function of L_S, respectively. (b) CDOD variation with LS across different latitudes; values are averaged within 5° latitude bins, and brighter colors indicate higher dust optical depth. Gray shaded regions mark L_S intervals where all variables exhibit peak values.

Variations in Solar Cycle. Over a nearly decade-long period, proton auroral intensity reflects a superposition of influences from solar longitude, solar activity, and dust storms. Beyond the prominent peaks near perihelion and the southern summer solstice, the remaining intensity trends closely follow EUV flux, decreasing during the declining phase of Solar Cycle 24 (2014–2019) and increasing during the ascending phase of Solar Cycle 25 (2020–2024). A concave pattern between enhanced intervals is evident in both EUV flux and dust activity, with its minimum near the southern winter solstice, suggesting that the Sun–Mars distance modulates auroral intensity, amplifying it when Mars is near perihelion.

Data gaps in MAVEN's record prevent full coverage of all six perihelion and solstice intervals, but three periods—Region I (1 Dec 2014–15 Apr 2015), Region II (13 Oct 2016–3 Jan 2017), and Region IV (18 Jul–24 Nov 2020)—contain sufficient data to identify distinct auroral patterns.

In the first half of Region IV, auroral intensity increased, similar to Region II, though both occurred during relatively weak EUV conditions. Region II exhibited a dip followed by recovery, aligned with dust storm activity; in contrast, Region IV showed a steady increase consistent with EUV variations, reinforcing the combined effects of both drivers. The latter half of Region IV resembles the post-solstice

decline seen in Region I, which occurred under strong EUV flux and exhibited higher overall intensity. This suggests that while seasonal timing near perihelion and solstice governs the general auroral pattern, solar activity remains a modulating factor. Moreover, the decline followed by a brief rebound in late Region IV mirrors dust storm variability during that period, further illustrating the role of dust and EUV in shaping auroral responses.

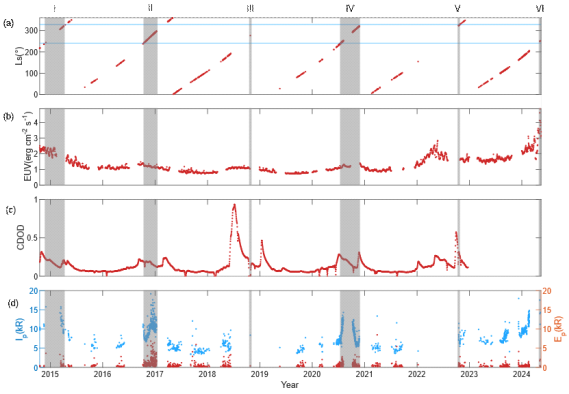

Figure 3. Long-term variations in proton auroral intensity and enhancement over nearly one solar cycle. The x-axis indicates the calendar year corresponding to all data used in this study. (a) Solar longitude (L_S) as a function of time. The region between the two blue lines marks the perihelion-to-southern summer solstice interval, repeated six times and shaded in gray. (b) Daily EUV flux, with data gaps due to missing entries in the MAVEN dataset. (c) Column dust optical depth (CDOD), available through December 2022. (d) Proton auroral intensity (blue dots, left y-axis) and enhancement (red dots, right y-axis). Auroral variations outside the shaded intervals generally follow EUV flux and CDOD trends, while those within the shaded regions are more strongly modulated by seasonal effects associated with solar longitude.

Conclusion and Discussion:

In this study, we investigated the variability of Martian proton aurorae across three characteristic timescales: the 26.35-day Carrington rotation, the seasonal cycle of one Martian year, and the nearly decade-long solar cycle.

On the Carrington rotation scale, we find that when solar wind speed, density, and dynamic pressure exhibit similar temporal patterns—whether peaks, rising trends, or declines—proton auroral intensity responds with corresponding variations. This behavior is primarily driven by enhanced ENA precipitation under increased dynamic pressure (Wang et al., 2018), with solar wind density showing the strongest correlation with auroral intensity. The aurora also responds sensitively to differences in amplitude even under otherwise similar conditions across rotations.

On seasonal timescales, peak proton auroral intensity and enhancement occur not only near the southern summer solstice, as previously reported (A. Hughes et al., 2019), but also during the perihelion interval preceding the solstice. A clear temporal sequence is observed: EUV flux peaks first, followed by increased CDOD, then by peaks in solar wind density and proton auroral activity.

Over the solar cycle, proton auroral intensity and enhancement follow an arc-like trend—weakening during the decline of Solar Cycle 24 and strengthening during the rise of Solar Cycle 25—consistent with EUV variations outside perihelion-solstice intervals. During perihelion and southern summer solstice, seasonal effects dominate, producing the strongest auroral responses, which are further amplified by concurrent EUV and dust activity. This study offers the first full-cycle characterization of proton auroral variability, enabled by a dataset twice the size of those used in previous studies (A. Hughes et al., 2019; A. C. G. Hughes et al., 2023).

Nonetheless, several questions remain. At the Carrington scale, only rotations 2184 and 2185 contain sufficient upstream solar wind and auroral data. Broader datasets are needed to assess the generality of the observed patterns. For seasonal variations, the influence of Hadley circulation—linked to Mars's hemispheric elevation contrast (Richardson & Wilson, 2002)—likely contributes to auroral enhancement, but the observed activity near perihelion suggests that the interplay between solar forcing and circulation warrants further study. For solar cycle effects, current data gaps limit comparison across all perihelion and solstice intervals.

Finally, future efforts should address nightside proton aurorae (Brinkfeldt et al., 2006), the role of horizontal magnetic fields in suppressing emissions (Gérard et al., 2019), and the global-scale variability indicated by patchy aurorae detected by EMUS (Henderson et al., 2022). On a global scale, patchy proton aurorae were detected by the Emirates Mars Ultraviolet Spectrometer (Atri et al., 2022; Chaffin et al., 2022; Holsclaw et al., 2021). Together, these results highlight the complex, multi-scale nature of Martian proton aurorae and the need for continued high-resolution, long-duration observations.

Data Availability Statement:

The MAVEN IUVS, SWIA, and EUV data are all publicly available at https://atmos.nmsu.edu/PDS/data/PDS4/MAVEN/. In this study, we use IUVS Level 1C version 13 altitude-binned periapsis data, SWIA Level 2 "onboardsvymon" data, and EUV Level 3 daily full spectrum data. The MEX ASPERA-3/IMA data is publicly available at https://amda.irap.omp.eu/desktop.php. The 9.3 μm absorption column dust optical depth data normalized to the gridded surface pressure value are publicly available through the Mars Climate Database (http://www-mars.lmd.jussieu.fr/mars/dust_climatology/index.html). The intensity and enhancement of proton aurora are publicly available at Wu (2025).

Acknowledgments:

This work was supported by the National Natural Science Foundation of China (Grant No. 42388101), the National Natural Science Foundation of China (42222408, 42441809), the National Key R&D Program of China (2021YFA0718600), the Youth Innovation Promotion Association of the Chinese Academy of Sciences (No.Y2021027), and the Postdoctoral Innovation Program of Shandong Province (SDCX-ZG-202502009). We would like to thank the entire IUVS, SWIA, and EUV team for providing data access and support. Special thanks to Ramstad, R., and Montabone, L. for their contributions in making available data from MEX and CDOD, respectively.